ORIGINAL PAPER

Evolution of primary phases and high-temperature compressive behaviors of as-cast AuSn20 alloys prepared by different solidification pathways

Qingbiao Tan · Chao Deng · Yong Mao · Guo He

Abstract The as-cast AuSn20 eutectic alloys prepared by four different solidification pathways have been investigated in terms of the microstructure and the high-temperature compressive behaviors. The primary phases appeared in the four alloys are very sensitive to the cooling rate, which decrease in the size and the volume fraction as the cooling rate increases. The morphologies of the primary ζ'-Au$_5$Sn phase are in dendritic at low cooling rate and change to rosette-like at high cooling rate. When the cooling rate is about 3.5×10^4 K/min, the primary ζ'-Au$_5$Sn can be suppressed but small δ-AuSn particles appear instead as the primary phase. The compressive behaviors at 220°C exhibit a low yielding stress and a long stress platform for the alloy prepared by injection casting with a copper crucible, which indicates an advantageous processing route for the production of the AuSn20 strips or foils.

Keywords AuSn20 alloy · Primary phase · Eutectic solidification · Rapid solidification · Hot working
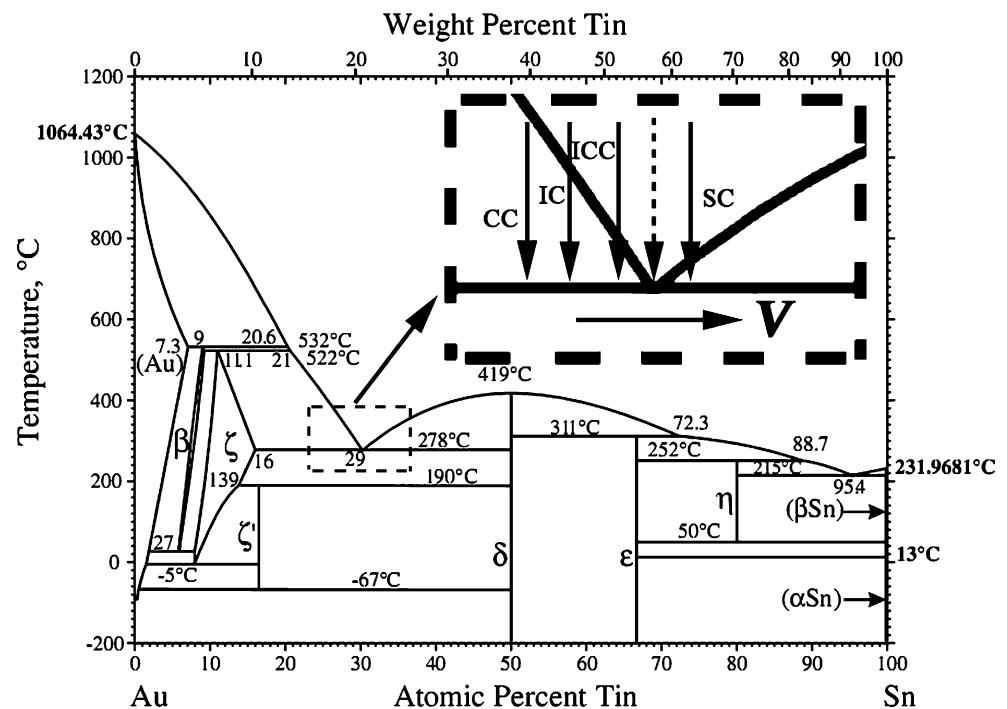
Introduction

Au-20 wt.% Sn eutectic solder alloy (denoted as AuSn20 hereafter) is extensively used in high power electronics and

Q. Tan · G. He (✉)
State Key Lab of Metal Matrix Composites, School of Materials Science and Engineering, Shanghai Jiao Tong University, Shanghai 200240, China
e-mail: ghe@sjtu.edu.cn

C. Deng · Y. Mao
Department of Materials Science and Engineering, School of Physical Science and Technology, Yunnan University, Kunming 650091, China

optoelectronics packaging due to its high-temperature performance, high mechanical strength, high electrical, and thermal conductivity [1–5]. Many studies of the AuSn20 solder are focusing on the soldering process, the microstructure evolution in the soldering joints [6, 7], and the solder alloy's performance [8–10]. Considering the manufacturing of this alloy, some unsolved problems still remain, such as the microstructure evolution in the processing and the mechanical behavior of the bulk AuSn20 solder alloy. It is well known that the miniaturization of microelectronic packages requires the bulk AuSn20 solder alloy to be very thin (usually 0.015–0.1 mm). Thermal rolling and/or room temperature rolling are usually preferred methods to reach the goal because the better surface quality of the thin alloy ribbons can be achieved by these processing routes. Generally, initial microstructure of the bulk AuSn20 alloy plays an important role in the rolling process. According to Au–Sn binary alloy phase diagram [11–13] as shown in Fig. 1, AuSn20 alloy should reveal a eutectic microstructure consisting of ζ'-Au$_5$Sn phase and δ-AuSn phase at room temperature. Both ζ' and δ are intermetallics with very hard and brittle nature. They lead to difficulties in the manufacture of the AuSn20 solder strips or foils. In practice, the nonequilibrium solidification usually results in forming primary dendritic ζ-Au$_5$Sn phase [6, 10]. The length scale and morphology of the dendrites are very critical to the mechanical properties of the alloy, which are always adverse to the manufacturing process. In order to refine the solidified microstructure, different solidification techniques can be used in the production of the bulk AuSn20 alloy. With those techniques various cooling rates during the solidification can be achieved. It is expected that rapid solidification [14, 15] will result in refined microstructure, extended solubility, reduced microsegregation, and forming metastable phases.

🙂 Springer

Fig. 1 Phase diagram for Au–Sn system and illustration of the optimal solidification path

The various initial microstructures must exhibit different plasticity and workability, which influence the manufacturing process of the thin alloy foil. This investigation will focus on the microstructure evolution and the compressive deformation behaviors of the as-cast AuSn20 alloy. Several casting methods are chosen because they can achieve different cooling rates. Our findings in this study are useful for optimizing the production of the AuSn20 solder foils.

Experimental procedures

The initial AuSn20 alloy was prepared in an electromagnetic induction furnace under argon atmosphere by melting pure gold plates (in purity of 99.999%) and tin particles (in purity of 99.99%) in a graphite crucible. Three different solidification techniques together with two kinds of mold with 5 mm in diameter were used to realize four different cooling rates. The detailed description and related data are listed in Table 1. A small piece of the alloy (about 0.06 g) was cut from the ingot for differential scanning calorimetry

(DSC) measurement and the DSC traces were obtained from 2920 MDSC under 1, 10, and 20 K/min, respectively. The samples for microstructure observation were cut at 3 mm from the bottom of the as-cast cylindrical ingots, and then prepared by standard metallographic technique without etching. The backscattering electric images were obtained by using a scanning electron microscopy (SEM) JEOL-JSM6460 with energy dispersive X-ray spectroscopy (EDS). The X-ray diffraction (XRD) patterns were taken from the cross-sections of each ingot by using a Bruker D8-ADVANCE diffractometer with CuKα radiation.

The microhardness measurements at room temperature were carried out by using a Vickers system, for which 100 g load and 15 s duration were applied and at least five random points were measured for each sample. The cylindrical specimens for the compressive test were prepared, which are 5 mm in diameter and 6 mm in length. Before testing, the specimens were heated to 220±2°C in a furnace and held for 5 min for homogeneity. The high-temperature compressive tests were performed by using an AG-100KNA ShimaDzu testing machine with a cross-head

Table 1 Four different solidification pathways and the corresponding cooling rates

Name	Casting methods	Cast mold	Casting temperature (°C)	Estimated cooling rate (K/min)
CC	Conventional casting	Graphite	330±5	2.4×10
IC	Injection casting	Graphite	~1100	4.2×10^2
ICC	Injection casting	Copper	~1100	9.0×10^3
SC	Suction casting	Copper with water cooling	~1700	3.5×10^4

speed of 5×10^{-4}/s. The maximum height reduction of the specimens is above 70%. After the test, the compressed disks were cut from the center parallel to the compression direction and the deformed microstructures were observed using SEM.

Results

The phase transition behavior under different heating and cooling rates

Figure 2 shows the melting and solidification behaviors of the AuSn20 alloy under different heating/cooling rates. The DSC traces reveal very similar onset temperatures in the heating routes with three different rates as shown in Fig. 2a. The two endothermic peaks are determined at about 190.1°C
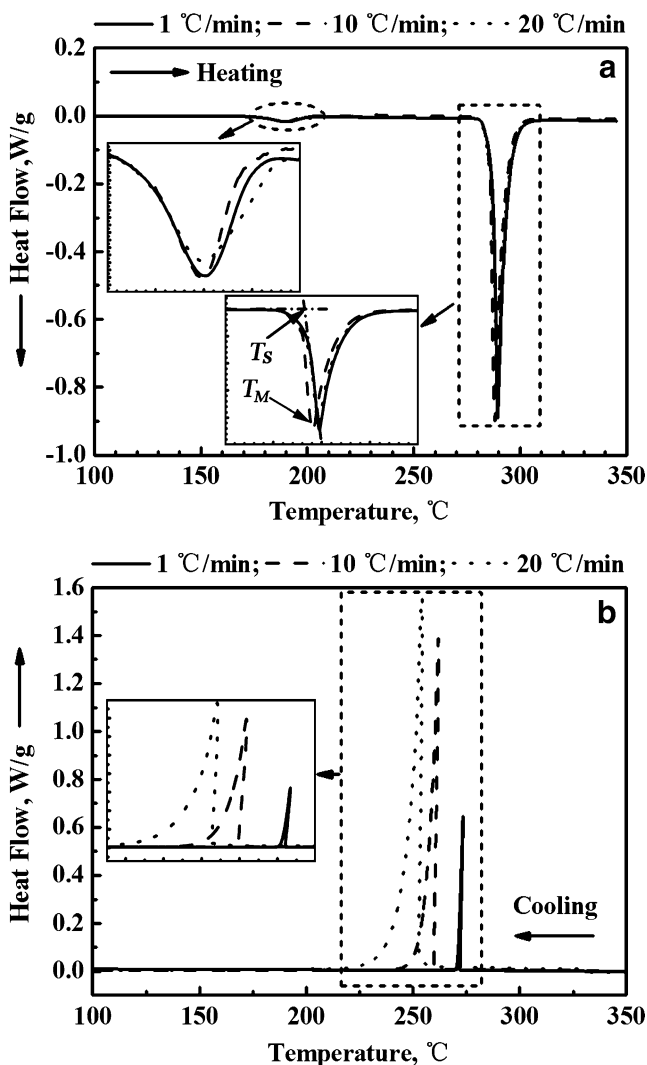

Fig. 2 DSC traces of AuSn20 eutectic alloy under different heating/cooling rates: **a** heating and **b** cooling

and 290°C. The first peak corresponds to the reverse peritectoid reaction $\zeta'+\delta\rightarrow\zeta$ or $\zeta'\rightarrow\zeta+\delta$ depending on the local Sn concentration [11–13]; the second peak corresponds to the melting reaction. The endothermic reaction around 190°C implies that the ordered-disordered transition $\zeta'\rightarrow\zeta$ is a first order phase transition. Some difference in the end temperatures of the solid–solid transition ($\zeta'\rightarrow\zeta$) between the different heating rates as shown in the inset in top left corner of Fig. 2a verifies that the structure transition is time-dependence.

Upon cooling, a sharp exothermic peak can be detected as shown in Fig. 2b, corresponding to the eutectic reaction $L\rightarrow\zeta+\delta$. But the following exothermic peritectoid reaction $\zeta+\delta\rightarrow\zeta'$ around 190°C cannot be detected. The start temperature of the solidification is significantly dependant on the cooling rates. For clarity, all the characteristic temperatures are summarized in Table 2. The supercooling temperature is defined as the difference between the end melting temperature and the onset solidification temperature. The higher cooling rate results in a greater supercooling.

As-cast microstructures under four different solidification pathways

Figure 3 presents the as-cast microstructure of the AuSn20 alloy under four different solidification pathways. The primary large dendrites with developed secondary arms (white phase) are evident for the CC pathway as shown in Fig. 3a, which are confirmed to be ζ'-Au_5Sn phase according to the EDS analysis (Table 3). The matrix is eutectic phase with typical irregular lamellar structure as shown in Fig. 4a. It is undoubted that the white phase is ζ'-Au_5Sn and the dark phase is δ-AuSn in the eutectic microstructure (Fig. 4a). For the IC pathway fine primary dendrites (ζ'-Au_5Sn phase) distribute in the eutectic matrix as shown in Fig. 3b. It is clear that the IC pathway provides higher cooling rate than the CC, and results in finer primary dendrites and eutectics. In addition, the volume fractions of the primary dendrites evidently differ between the two methods (Fig. 3a and b). Higher cooling rate (IC) leads to smaller volume fraction of the primary dendrites (compared with CC). In virtue of the image analysis, the volume fractions of the primary dendrites are estimated to be 30±5% for CC and 15±5% for IC, respectively. When the ICC pathway (with much higher cooling rate) is applied, the primary dendrites are much finer as shown in Fig. 3c. Their volume fraction can be estimated to be 7±3% which is much smaller than that of IC or CC. It is noticeable that the dendritic morphology of ICC reveals a different feature from other two samples (IC and CC). Such ripened equiaxed dendrites (Fig. 3c) was named as "rosette" [16].

Table 2 Characteristic temperatures of AuSn20 alloy determined from the DSC traces

Heating/cooling Rate (K/min)	Heating						Cooling		
	Solid–solid transformation			Solid–liquid transformation			Liquid–solid transformation		
	T_S (°C)	T_M (°C)	ΔH (J/g)	T_S (°C)	T_M (°C)	ΔH (J/g)	T_S (°C)	ΔH (J/g)	ΔT (°C)
1	179.4	190.5	1.50	287.1	289.5	28.77	273.4	29.00	16
10	181.3	190.0	1.45	285.8	288.2	29.17	261.8	28.63	26
20	178.6	190.2	1.56	286.8	289.4	28.15	256.7	27.25	33

When SC pathway with extremely high cooling rate is applied, the primary phase ζ′-Au₅Sn is completely restrained. The δ-AuSn instead nucleates and grows in the initial solidification, forming irregular polygonal particles as shown in Fig. 3d. The size of the primary δ-AuSn particles is in about several microns, and their volume fraction can be estimated to be about 5±3%. A careful observation has confirmed that the small particles disperse in the eutectic matrix homogeneously through all the section of the as-cast cylinder. Figure 4b shows some details of the eutectic structure where the primary δ-AuSn particles (in dark) act as nucleuses of the eutectic growth and lead to a radial-columnar or lamellar eutectic structure. Compared with the CC (Fig. 4a), the lamellar spacing of the SC eutectic structure is smaller, indicating that the higher cooling rate also refines the eutectic microstructure.

Considering the total phase percentages in the as-cast AuSn20 alloy, one can easily estimate the ζ′-Au₅Sn phase in about 65% (total of the primary phase and that in the eutectic, supposing 50% ζ′+50% δ in the eutectic) and δ-AuSn in about 35% for the CC alloy. The ζ′-Au₅Sn phase decreases in total percentage as the cooling rate increases (such as IC and ICC alloys) and the δ-AuSn phase tends to increase. For the SC alloy cast under extremely high cooling rate, the percentage of the δ-AuSn phase (about 52.5%) becomes larger than that of the ζ′-Au₅Sn phase (about 47.5%). XRD patterns (shown in Fig. 5) have evidently verified such relationship between the solidified phases and the casting pathways (cooling rates). The strong peaks correspond to the ζ′-Au₅Sn phase for the CC alloy (Fig. 5), suggesting that the ζ′-Au₅Sn phase is dominant. But for the SC alloy, the strong peaks corresponding to the δ-AuSn phase suggest that the δ-AuSn is dominant in the microstructure.

Microhardness at room temperature

Although both ζ′-Au₅Sn and δ-AuSn are intermetallics with hard and brittle nature, the mixture of the two phases with

Fig. 3 As-cast microstructures of the AuSn20 alloy showing different primary phases under different solidification pathways: **a** CC, **b** IC, **c** ICC, and **d** SC
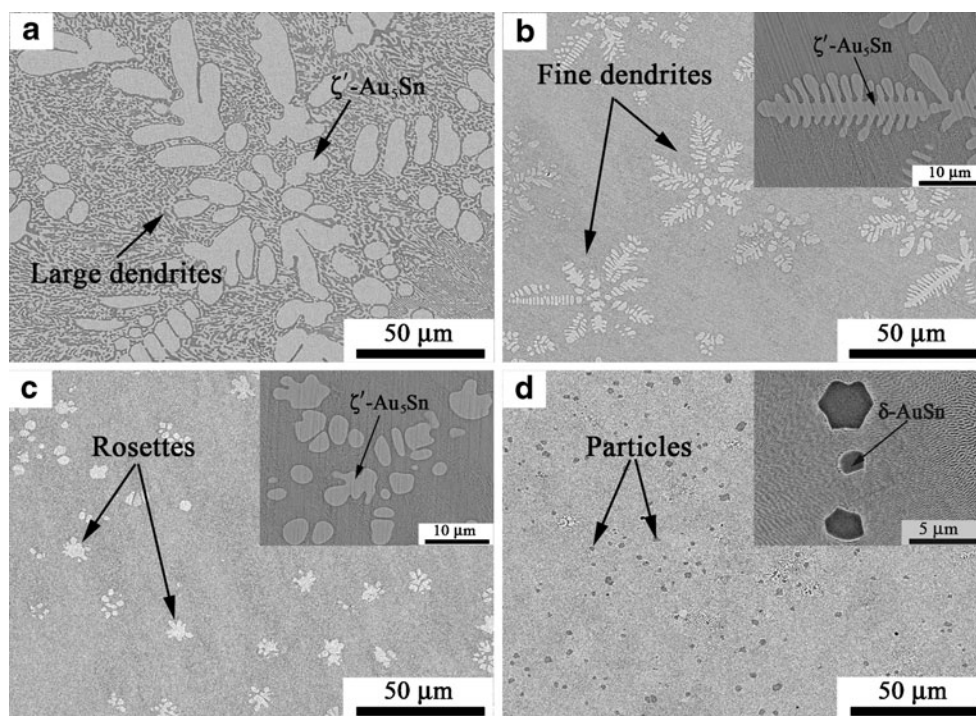
Table 3 Concentrations (wt.%) of the primary phases measured by EDS analysis

Casting methods	Au	Sn	Suggested phases
CC	90.3	9.7	ζ'-Au$_5$Sn
IC	90.5	9.5	ζ'-Au$_5$Sn
ICC	91.1	8.9	ζ'-Au$_5$Sn
SC	62.7	37.3	δ-AuSn

different percentages and various grain geometry and size may result in very different mechanical properties. The microhardness of the as-cast AuSn20 alloys tested at room temperature is listed in Table 4. Some reported data [9, 10, 17, 18] are also collected in the table for comparison. As expected CC alloy exhibits the lowest hardness (HV138) and ICC alloy has the highest hardness (HV219) in the three tested samples. Since the 100 g load was applied in Vickers measurements, the width of the indentation was large enough to span many eutectic domains and some primary dendritic/rosette phases. Each tested hardness value is the average of the local eutectics and the primary phase. It is clear that the tested hardness depends on the local eutectic microstructure and the phase hardness. In general, eutectic phases with a very fine lamellar microstructure have higher hardness than the primary phase. The CC alloy
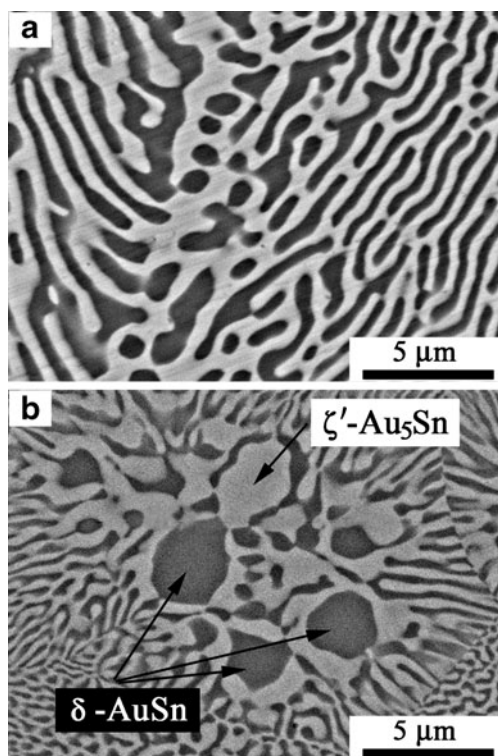
Fig. 4 Eutectic microstructures of the as-cast AuSn20 alloy: **a** irregular lamellar eutectics in CC alloy and **b** irregular equiaxed eutectic grain in SC alloy
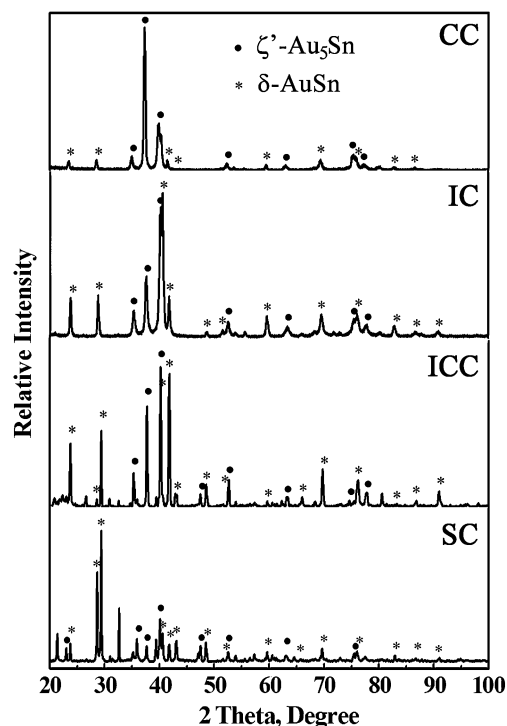
Fig. 5 XRD patterns of the as-cast AuSn20 alloys under different solidification pathways

with the largest volume fraction of the primary phase exhibits the lowest hardness, while the ICC alloy with the smallest volume fraction of the primary phase exhibits the highest hardness among the three tested samples. Besides, the phases solidified under high cooling rate usually exhibit higher hardness than that solidified under low cooling rate because of the nonequilibrium solidification. This also contributes to the tested hardness values.

Table 4 Microhardness values of the as-cast AuSn20 alloys

Source	Cooling rates / status	Hardness (HV)
CC	2.4×10 K/min	138±4
IC	4.2×10^2 K/min	207±5
ICC	9.0×10^3 K/min	219±3
[9]	Air cooling	~173 (global microhardness)
[10]	Slowly solidification	177±7, 10 g (ζ'+δ eutectics)
		143±3, 10 g (ζ'-Au$_5$Sn)
		107±1, 10 g (δ-AuSn)
[17]	Solid-state aging of diffusion couples	123±19 (ζ'+δ eutectics)
		236±19 (ζ'-Au$_5$Sn)
		104±6 (δ-AuSn)
[18]	Electrodeposition (fine grain)	211±29 (ζ'+δ eutectics)
		178±16 (ζ'-Au$_5$Sn)
		199±19 (δ-AuSn)

Some published data are presented for comparison
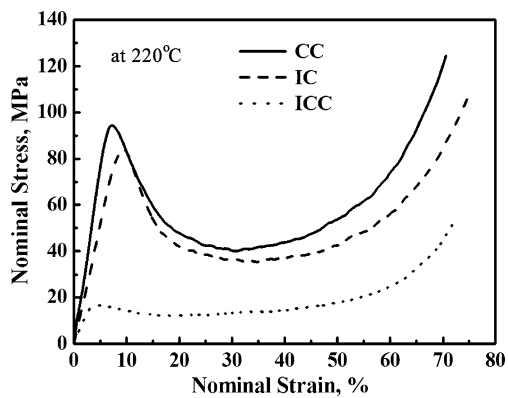
Fig. 6 High-temperature compressive stress–stain curves of the as-cast AuSn20 alloys

Fig. 7 Plot of the cooling rate to the characteristic compressive properties at 220°C for the AuSn20 alloys

Compressive behaviors at high temperature

The high temperature compressive tests were carried out at starting temperature 220°C which is about 30°C higher than the order–disorder transition temperature. The microstructure of the tested alloy is composed of primary ζ-Au$_5$Sn and eutectic ζ-Au$_5$Sn+δ-AuSn at the testing temperature. The disordered ζ-Au$_5$Sn has a Mg-type close packed hexagonal structure which is supposed to be easily deformed compared with the ordered ζ′-Au$_5$Sn.

The high temperature compressive stress–strain curves of the tested alloys exhibit typical three stage behaviors, i.e. initial elastic strain, yielding and plastic strain accompanying dynamic recrystallization, and the final densification as shown in Fig. 6. We are amazed to see that the yielding strength is 94 MPa for CC and 84 MPa for IC, but only 17 MPa for ICC. This suggests that the size and the volume fraction of the primary phase ζ-Au$_5$Sn play a significant role in strengthening. If there is no primary phase in the microstructure, the eutectics may exhibit very small deformation resistance. Under this situation the AuSn20 alloy will become easily forged or rolled.

At the stage of the plastic deformation a distinct strain softening occurs due to the dynamic recrystallization for the CC and IC alloys, leading to a sharp decrease in the flow stress. After then, a short stress platform appears followed by a quickly stress increase (Fig. 6). In a different manner, the ICC alloy exhibits a long low-stress platform in the stress–strain curve, which indicates that the effect of work-hardening is well balanced by the dynamic recrystallization. Compared the ICC with the CC and IC, one can consider that the primary phase counts for much in the stress–strain behavior. For clarity, all the mechanical data determined from the stress–strain curves are summarized in Fig. 7. Obviously, the eutectic AuSn20 with little or without the primary phase is highly advantageous to the rolling processing in the strips or foils production because of its
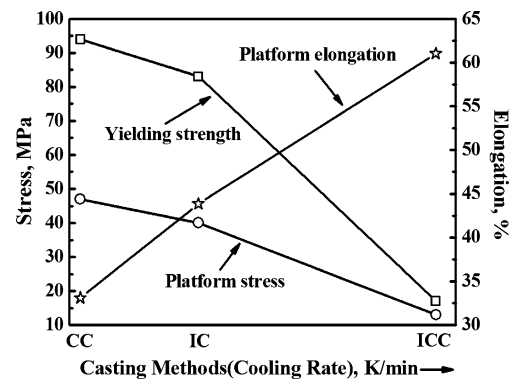
lower yielding stress, longer stress platform, and larger plastic strain. After the severe plastic deformations, the AuSn20 strips or foils can be improved in chemical homogeneity, which provides good, steady package properties for the soldering applications.

Discussion

Primary phases for different solidification pathways

The crucial difference among the four solidification pathways is the cooling rate (Table 1). It is well known that the solidified microstructure can be refined when a large cooling rate is applied. The DSC measurements (Fig. 2b) have validated that the large cooling rate induces a large supercooling. According to the solidification principles [19], the nucleation rate and the growth rate in the supercooled melt are controlled by both thermodynamic and kinetic conditions. Under small supercooling (normal casting process, e.g., CC and IC in this study), the diffusion-controlled dendritic growth depends on the cooling rate. Its size becomes small as the cooling rate increases, because the growing up of the dendrites is kinetically suppressed in large cooling rate (Fig. 3b). Under large supercooling (rapid solidification, e.g., ICC and SC in this study), solidification occurs at very low temperatures, so that the nucleation rate is significantly improved but the grain growth is restrained due to the limited atoms diffusion. The rapid solidification must results in very fine primary phases (Fig. 3c and d) and fine eutectic structure (Fig. 4b). These phenomena were also found in the reflow joint of the AuSn20 solder [6] and other eutectic [14] or hypereutectic alloys [20]. For quantitative description, the measured characteristic sizes of the primary phases for the four solidification pathways are presented in Fig. 8, which clearly shows the significant cooling rate dependence of the primary phases.
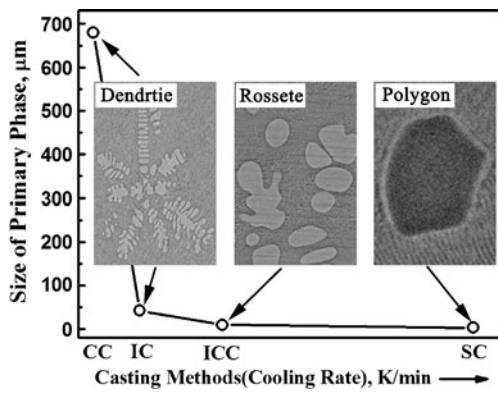
Fig. 8 The characteristic sizes of the primary phases for the four solidification pathways

Besides the size, the morphology of the primary phase is also sensitive to the cooling rate. The developed first arms of the dendrites will become short and tend to evolve into the ripened equiaxed dendrites, i.e., rosette, as the cooling rate increases from about 4.2×10^2 K/min (IC) to about 9×10^3 K/min (ICC). Based on these observations, a distinct tendency can be depicted that as the cooling rate increases the primary phase size and its volume fraction decrease, and the developed dendrites become small dendrites and even small rosettes. A critical cooling rate must exist under which the primary phase disappears. This critical cooling rate can be estimated between 9.0×10^3 K/min (corresponding to ICC pathway) and 3.5×10^4 K/min (corresponding to SC pathway) as illustrated with a dashed arrow in Fig. 1 according to this study. Figure 9 has illustrated such evolution of the primary phase in the AuSn20 alloy. These phenomena have also been observed in other eutectic or hypereutectic alloys [20, 21].

It is interesting that the δ-AuSn phase solidifies primarily when the cooling rate is high enough to suppress ζ-Au$_5$Sn, e.g. SC pathway. The primary δ-AuSn phase prefers growth in faceted manner (insert in Fig. 3d). Because the primarily
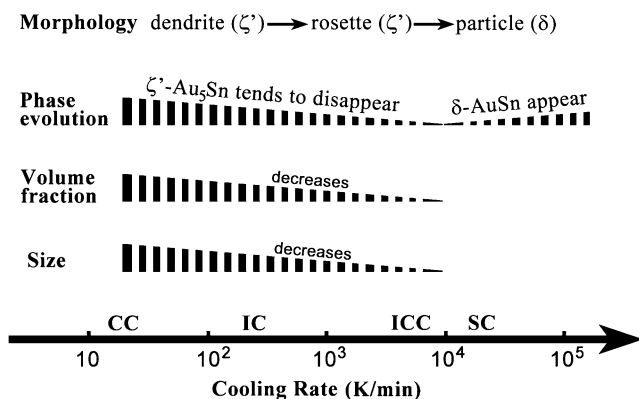

Fig. 9 The cooling rate-dependence of the primary phases of the AuSn20 alloy

solidification occurs under large supercooling, a high nucleation rate is expected for the rapid solidification, which contributes to the refinement of the microstructure. Unlike dendritic growth with a continuous mode, the faceted grain growing via noncontinuous mechanism has a slow growth velocity, and then tends to form small particles (Fig. 3d).

Effect of the initial microstructure on the high temperature compressive behaviors

It is well known that the yielding strength of metallic materials depends on their microstructure. High cooling rate during solidification generally leads to fine microstructure, resulting in high yielding strength (Hall–Petch relation). Besides, rapid solidification restrains atoms diffusion to induce a high concentration of defects (e.g., voids, dislocations, etc.) in the crystals, which can enhance the deformation resistance and contribute to the yielding strength. According to above discussions, the as-cast AuSn20 alloys should exhibit yielding stresses at room temperature in following turns:

$$\sigma_{CC} < \sigma_{IC} < \sigma_{ICC} \, (\text{at room temperature})$$

Although the room temperature compressive test cannot be operated due to the brittle nature of the alloy, the microhardness measurements (Table 4) at room temperature have indirectly verified the above estimation. It is interesting to find that the high temperature yielding strength under compressive stress is in a reverse sequence (Fig. 6):

$$\sigma_{CC} > \sigma_{IC} > \sigma_{ICC} \, (\text{at } 220^\circ C)$$

It is undoubted that some microstructure evolution has occurred during the heating and the 5 min holding at 220°C. According to Au–Sn binary phase diagram (Fig. 1 [11–13]), the ordered–disordered transition ($\zeta' \rightarrow \zeta$) has already finished at such high temperature. But this should not be the crucial reason that induces such difference in the yielding stress. The eutectic matrix is probably the source that can be utilized to modulate the mechanical properties of the AuSn20 alloy. The lamellar eutectics have a thermodynamic tendency of globularizing at high temperature because of the high interfacial energy. The initial eutectics formed under different supercooling, which are in different refinements of the lamellar spacing (Fig. 4), have different driving force for the eutectic evolution. Among the three alloys the ICC has the largest driving force, thus induces the largest falling of the yield stress (Fig. 6). Besides, the composite of the primary dendrites and the eutectics can significantly improve the yielding stress. The CC with the largest volume fraction of primary dendrites has the strongest "composite-effect," thus exhibits the largest yielding stress (Fig. 6). In addition, the average compositions of the eutectics are different

among the three alloys due to different volume fractions of the primary phases. This should also influence the eutectic evolution and the yielding stress.

After yielding, the continuous plastic strain has induced dynamic recrystallization in the eutectics. If the strain-hardening is roughly balanced by the recrystallization a stress platform can be maintained (ICC alloy shown in Fig. 6). As the strain progresses, the dynamic recrystallization impairs the "composite-effect" because the dendrites are broken and inclined towards the plastic flow orientation (Fig. 10a and b), so that a rapid decrease in the stress after the yielding can be observed. When the "composite-effect" is exhausted, a short stress platform appears (CC and IC alloys shown in Fig. 6). For the ICC alloy, the small "rosettes" have mixed with the recrystallized eutectic matrix (Fig. 10c), there is almost no such "composite-effect." After the high temperature compressive test, all the lamellar eutectics transform into a dual phases microstructure with granular grains (via globularization mechanism [22]) where the δ-AuSn islands are isolated by the ζ'-Au$_5$Sn matrix as shown in Fig. 10d. Such globularization behavior is a typical dynamic recrystallization [22].

So far, there are many eutectic alloys [23–26] which were found to exhibit superplasticity at certain temperature or conditions. Does the AuSn20 eutectic alloy also exhibit superplasticity? If it does, in which conditions the super-plasticity appears? This work has displayed the possibility of superplasticity in AuSn20 eutectic alloy. The ICC alloy with fine eutectic microstructure and little primary phase exhibits a longer low-stress platform at about 220°C, which is promising to exhibit superplasticity. In the next work, the special attention should be paid on the strain rate dependence of the plasticity, restriction of the primary phase, and refinement of the eutectic phases.

Conclusions

The AuSn20 eutectic alloy tends to form primary phase and then eutectic phases during solidification. The primary phase is very sensitive to the cooling rate. With the conventional casting pathway by which the cooling rate is about 24 K/min, the primary phase is in dendritic, and the solidified microstructure is composed of the primary dendritic ζ'-Au$_5$Sn and the lamellar eutectic ζ'-Au$_5$Sn+δ-AuSn. As the cooling rate increases, the primary dendrites become small in both the size and the volume fraction, and their morphology becomes rosette-like. If the cooling rate is large enough (e.g., 3.5×10^4 K/min) the primary ζ'-Au$_5$Sn can be suppressed but small δ-AuSn particles appear instead as the primary phase.

The as-cast AuSn20 alloys exhibits three stage stress–strain behaviors under compressive stress at 220°C, which is the elastic strain, the yielding and the plastic strain accompanying dynamic recrystallization, and the final densification. Although the room temperature microhardness of the alloys increases as the cooling rates increase, the yielding stress at 220°C displays a significant decrease due

Fig. 10 The oriented dendrites and the recrystallized micro-structure of the lamellar eutectics after high temperature compressive deformation. **a** CC, **b** IC, **c** ICC, and **d** the recrystallized microstructure of the CC eutectics
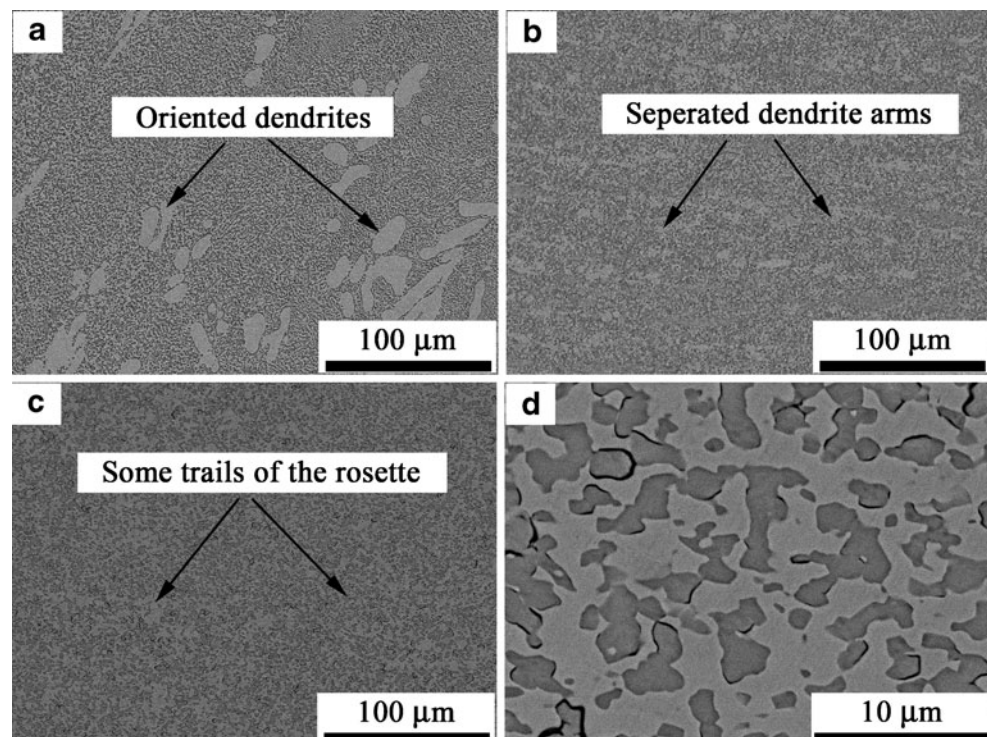
to the eutectics relaxation. The CC and IC alloys exhibit a rapid stress falling after yielding because the "composite-effect" impairs during the plastic strain. The ICC alloy exhibits a very low yielding stress and a longer stress platform because the strain-hardening can be well balanced by the dynamic eutectic recrystallization. This finding suggests that ICC pathway is beneficial to the production of the AuSn20 strips or foils.

References

1. Tan CW, Chan YC, Leung B, Liu HD (2008) Opt Lasers Eng 46:75
2. Pittroff W, Erbert G, Beister G, Bugge F, Klein A, Knauer A, Maege J, Ressel P, Sebastian J, Staske R, Traenkle G (2001) IEEE Trans Adv Packag 24:434
3. Zhao J, Li L, Wang WM, Lu YC (2003) IEEE Photon Technol Lett 15:1507
4. Qu Y, Yuan S, Liu CY, Bo BX, Liu GJ, Jiang HL (2004) IEEE Photon Technol Lett 16:389
5. Liu XS, Hu MH, Nguyen HK, Caneau CG, Rasmussen MH (2004) IEEE Trans Adv Packag 27:640
6. Chung HM, Chen CM, Lin CP, Chen CJ (2009) J Alloy Compd 485:219
7. Tsai JY, Chang CW, Shieh YC, Hu YC, Kao CR (2005) J Electron Mater 34:182
8. Zhang GS, Jing HY, Xu LY, Wei J, Han YD (2009) J Alloy Compd 476:138
9. Liu YC, Teo JWR, Tung SK, Lam KH (2008) J Alloy Compd 448:340
10. Bergmann R, Tang PT, Hansen HN, Moller P (2007) *Proc. 9th electronics packaging technology conference*, Singapore
11. Matijasevic GS, Lee CC, Wang CY (1993) Thin Solid Films 223:276
12. Okamoto H, Phase J (2007) Equilib Diff 28:490
13. Ciulik J, Notis MR (1993) J Alloy Compd 191:71
14. Gao Q, Guo JT, Huan KW (2007) Intermetallics 15:734
15. Sheng LY, Zhang W, Guo JT, Ye HQ (2009) Mater Charact 60:1311
16. Tzimas E, Zavaliangos A (2000) Mater Sci Eng A289:217
17. Chromik RR, Wang DN, Shugar A, Limata L, Notis, Notis MR, Vinci RP (2005) J Mater Res 20:2161
18. Vicenzo A, Rea M, Vonella L, Bestetti M, Cavallotti PL (2004) J Sol State electrochem 8:159
19. Chalmers B (1964) Principles of Solidification. Wiley, New York, p 150
20. Xu CL, Jiang QC (2006) Mater Sci Eng A437:451
21. Xu CL, Wang HY, Qiu F, Yang YF, Jiang QC (2006) Mater Sci Eng A417:275
22. Semiatin SL, Seetharaman V, Weiss I (1999) , Mater Sci Eng A263:257
23. Sundar RS, Kitazono K, Sato E, Kuribayashi K (2001) Acta Mater 49:1717
24. Ha TK, Chang YW (1999) Scr Mater 41:103
25. Uan JY, Lui TS, Chen LH (1996) Mater Chem Phys 43:278
26. Moles MDC, Davies GJ (1976) Scr Metall 10:455